Section 2

Data sets, diagnostic and dynamical investigations, statistical post-processing , multi-year reanalyses and associated studies

A multi-decadal climatology of North Pacific Polar Lows Employing Dynamical Downscaling

FEI CHEN[1], BEATE GEYER[1], HANS VON STORCH[1] ,MATTHIAS ZAHN[2]

[1] Institute of Coastal Research, Helmholtz-Zentrum Geesthacht, Germany

[2] University of Reading, Harry Pitt Building, Reading, U.K.

The North Pacific is an area where frequently sub-synoptic Polar Lows form in the winter season, especially over the Japan Sea, Bering Sea and Gulf of Alaska. We employed a dynamical downscaling method for constructing realistically the formation and life cycles during the past decades without exploiting sub-synoptic information in initial fields. A regional climate model is conditioned by large-scale information of NCEP re-analyses data.

The method consists of running a regional climate model (RCM) on the North Pacific Ocean region, and dynamically downscaling the NCEP 1 re-analysis data (Kalnay et al., 1996) for 1949 to 2010. A first study has shown that realistic Polar Lows are formed in the simulation with more detail than in the driving NCEP re-analysis (Chen et al., 2012).

Model used

All the initial and boundary conditions were provided by the NCEP 1 re-analysis data. The large-scale constraining technique in which known as spectral nudging (von Storch *et al.,* 2000) has been used in order to keep the large scale variability close to the NCEP re-analysis, which is available four times a day, and is interpolated to the shorter model time step. We applied this nudging at 750hPa and above, it goes stronger with height. It is limited to horizontal wind velocities and spatial scales larger than 800km.

Tracking Polar Lows

The detection and tracking-algorithm previously developed by Zahn and von Storch (2008a), for finding Polar Lows in the output of COSMO-CLM simulations works in three steps: First the local minima are identified in the band-pass filtered mean sea level pressure field. In the second step the detected positions of pressure minima are combined time-step by time-step to form tracks. In the final third step, some constraints are employed to remove remaining synoptic cyclones. We modified some of the fulfilled parameters to adapt the North Pacific.

Results

Figure 1 a shows the yearly time series of the number of detected polar lows per polar low season (PLS) from October to April. The mean number is 184 polar lows for each PLS with a strong year-to-year variability indicated by a standard deviation of approximately 31. Maximum and minimum numbers of detected cases are found in PLS 1969 with 258 cases and 2008 with only 137 cases. The decadal variability is weak. The overall trend in the frequency of polar lows is positive with

0.675 cases/year. The annual cycle of monthly numbers of detected polar lows reveals highest frequency in winter with maxima in December and January and almost no polar low activity in summer (not shown).

The spatial distribution of polar low occurrences is plotted in Figure 1 b. The location of each polar low is defined as the location at which its track is detected for the first time. Highest absolute frequency and frequency per maritime area are found in the region of Japan Sea in accordance with investigation of *Yarnal et al.* By a collection of 7 winter seasons Defence Meteorological Satellite Program (DMSP) infrared imagery, Yarnal concluded that the most active polar low cyclogenesis takes place in the western extratropical North Pacific, with the greatest rates of formation found east of northern Japan. A second maximum in counts per maritime area unit is found in the south-west of Bering Sea and the Gulf of Alaska.

By a Canonical Correlation Analysis (CCA) between the polar low density and mean sea level pressure field (not shown), we were able to detect links to large scale pressure patterns. We determined MSLP patterns, averaged across a polar low year, which favour or disfavour the formation of spatial polar low occurrence. Southward or pole-ward mean flows were found to establish large-scale time mean environments with which less or more polar lows develop. Details will be reported in a forthcoming article.

In this study, the model did not reproduce all polar lows observed in reality ; however, relevant statistics of polar low dynamics are realistically reproduced – in particular the number of polar lows, their spatial distribution and the link to the large scale MSLP field.

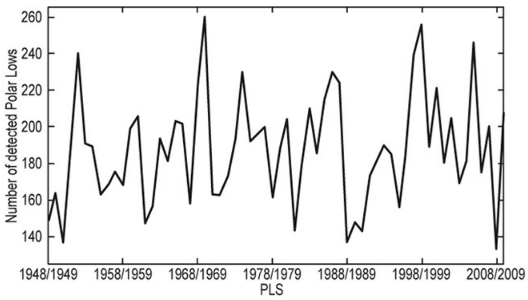

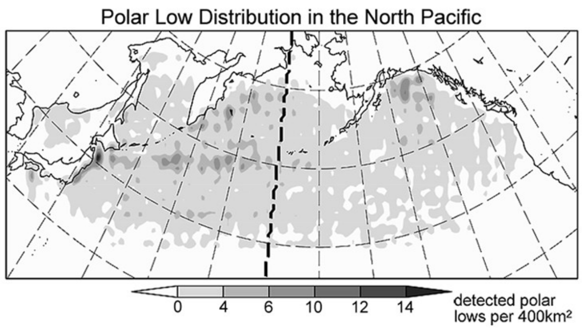

Figure 1. a) Number of detected polar lows per polar low season. One polar low season is defined as the period starting 1 October and ending 30 April the following year. b) Polar low density distribution. Unit:detected polar lows per 400 square kilometres.

Reference

Chen, F., B. Geyer, M. Zahn, and H. von Storch, 2012: Toward a multi-decadal climatology of North Pacific Polar Lows employing dynamical downscaling. Terr. Atmos.Ocean. Sci., **23**, 27-35, doi: 10.3319/TAO.2011.11.02.01(A)

Kalnay,E., M. Kanamitsu, R.Kistler, W.Collins, D.Deaven, L.Gandin, M.Iredell, S.Saha, G.White, J.Woollen, Y.Zhu, M.Chelliah, W.Ebisuzaki, W.Higgins, J.Janowiak, K.Mo, C.Ropelewski, J.Wang, A.Leetmaa, R.Reynolds, R.Jenne, D.Joseph, 1996: The NCEP/NCAR re-analysis project. *Bull. Amer. Meteor. Soc.* **77**,437-471.

von Storch, H., H. Langenberg, and F. Feser, 2000. A spectral nudging technique for dynamical downscaling purposes. *Mon. Wea. Rev*. **128**,3664-3673.

Yarnal, B., and K. G. Henderson, 1989. A Climatology of Polar Low Cyclogenetic Regions over the North Pacific Ocean. *J. Climate*. **2**, 1476–1491.

Zahn, M., and H. von Storch, 2008a. Tracking Polar Lows in CLM. *Meteorol. Z.*, **17(4)**, 445-453.

Zahn, M., and H. von Storch, 2008b. A longterm climatology of North Atlantic Polar Lows. *Geophys Res. Lett.*, **35, L22702**, doi:10.1029/2008GL035769.

Verification of high resolution ensemble forecasts using the 4-dimensional Fractions Skill Score

Le Duc[12], Kazuo Saito[21], and Hiromu Seko[21]

[1]Japan Agency for Marine-Earth Science and Technology, Yokohama, Japan; leduc@jamstec.go.jp

[2]Meteorological Research Institute, Tsukuba, Japan

We conducted two 11-member ensemble prediction systems MF10km and MF2km with the resolutions of 10 km and 2 km, the later nested inside the former with a 6-hour lag, for 15 days in the summer of 2010. The two ensemble systems were verified to examine the value of cloud-resolving ensemble forecast in predicting small spatiotemporal-scale precipitation. Therefore we focused on short time (1-hour) rainfall with a small scale (5 km) verification grid. The domains of the two systems and the verification area are shown in Fig. 1.

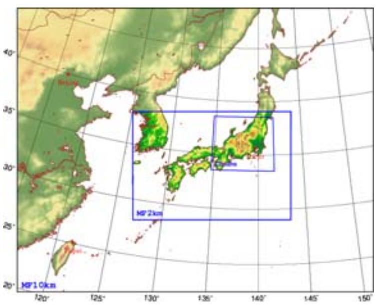

Fig. 1. Domains of MF10km and MF2km and verification area.

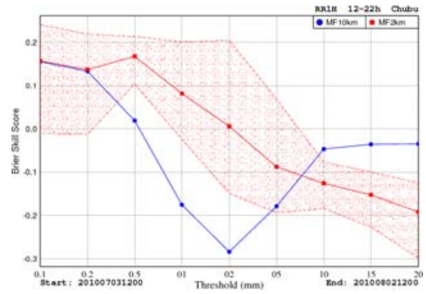

Fig. 2. BSS of hourly precipitation forecasts from MF10km and MF2km.

Since the verification was performed on short-term precipitation at high resolution, uncertainties from small-scale processes in space and time caused the traditional verification methods inconsistent with the subjective evaluation. This is illustrated in Fig. 2 and Fig. 3 in which the Brier Skill Scores indicate that two systems had no skills with respect to moderate and heavy rain, whereas the “eyeball” verification did not.

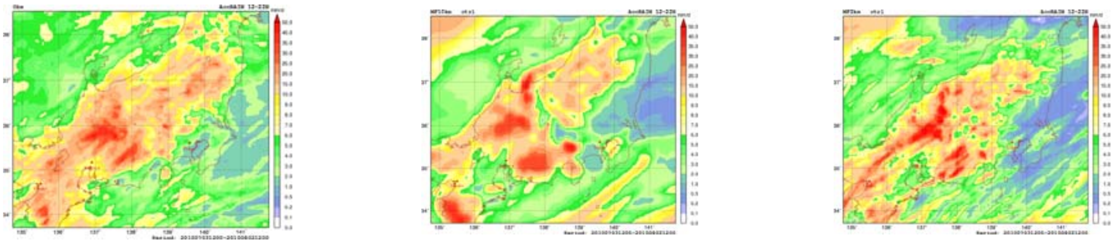

Fig. 3. Rainfall analysis (left) and corresponding forecasts by MF10km (center) and MF2km (right) controls (the average rainrates, unit mm d^{-1}, are shown in the plot).

The fall of the traditional verification methods with high resolution precipitation forecasts is attributed to the fact that the short predictability of small-scale processes in space and time was not taken into account in these methods. This problem remains even in the ensemble forecast if the verification grid size is small. In recent year, a number of new verification methods were proposed to account for spatial mismatches between deterministic forecasts and observations. However, not many studies were performed on the time lag issue. The other issue is how to apply the spatial verification methods into ensemble forecast. In this study, we introduced an extended verification method based on the Fractions Skill Score (FSS) by Roberts and Lean (2008) to account for these uncertainties. The main idea is to extend the concept of spatial neighborhood in FSS to the time and ensemble dimension.

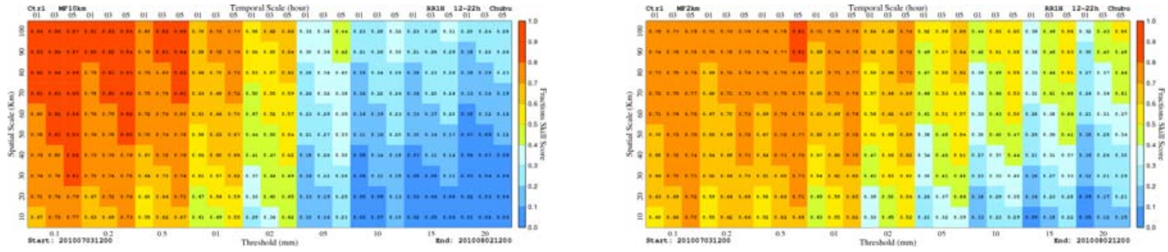

Fig. 4. Intensity-scale diagrams with temporal scales incorporated.

The incorporation of the time dimension into FSS requires a new form for intensity-scale diagrams. For each intensity value in the intensity-scale diagram, an additional horizontal temporal scale axis will be embedded. This new intensity-scale diagram is given in Fig. 4. In this figure, FSS-constant lines with a slope of -20 km / 2 hour can be identified in each spatial-temporal sub-diagram, indicating that the FSS values at small spatial and long temporal scales are equal to the ones at large spatial and short temporal scales. This reveals the important role of temporal scales in short-term precipitation verification at small spatial scales.

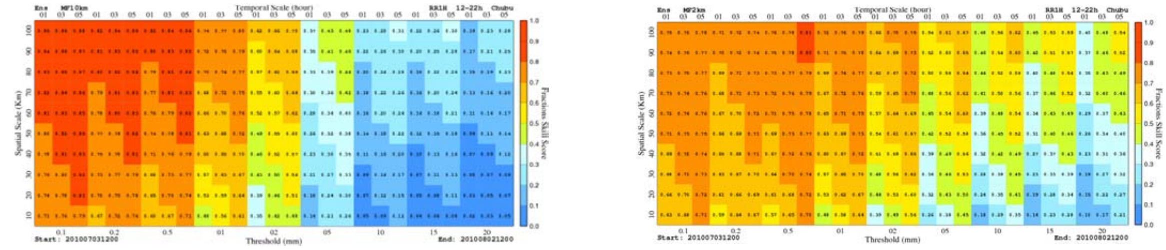

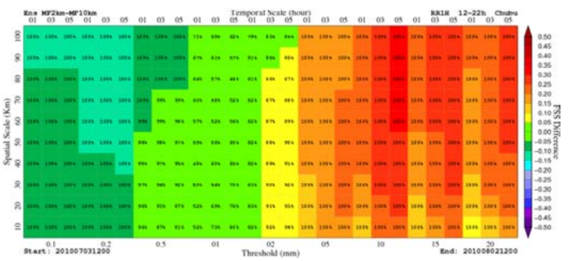

Fig. 5. Extended intensity-scale diagrams showing FSSs from MF10km (top left) and MF2km (top right) hourly precipitation forecasts and their differences (bottom left).

The performances of two systems as measured by the extended FSS are shown in Fig. 5. MF2km clearly outperforms MF10km in predicting heavy rain. In contrast, MF10km is slightly better than MF2km with respect to light rain. Two systems have the same performance with respect to moderate rain. The fact that the lower-resolution forecasts MF10km were better than the high-resolution forecasts MF2km for light rains suggests that the horizontal resolution of 2 km is not necessarily fine enough to completely remove the convective parameterization.

In addition to the FSS, the neighborhood concept was also incorporated to reliability diagrams and relative operating characteristics to verify the reliability and resolution of two systems. In verification of MF2km, the reliability and resolution with spatial lag of 20 km and the temporal scale of 1 hour was almost the same that with temporal lag of 2 hours and the spatial scale of 10km (not shown here).

Reference

Roberts, N. M., and Lean H. W., 2008: Scale-selective verification of rainfall accumulations from high-resolution forecasts of convective events. *Mon. Wea. Rev.*, **136**, 78–97.

Development of Extreme Weather Warning Products
with JMA One-month Ensemble Prediction System

Masashi Harada and Yuhei Takaya
Climate Prediction Division, Japan Meteorological Agency
E-mail: m_harada@met.kishou.go.jp

1. Introduction

The Climate Prediction Division of the Japan Meteorological Agency (CPD/JMA) is currently developing a number of extreme weather warning products based on the operational one-month ensemble prediction system (EPS). For these products, the Extreme Forecast Index (EFI) developed at ECMWF (Lalaurette, 2002; 2003) is adopted to indicate how and where EPS forecasts differ from the climatological probability distribution. In this short report, we briefly describe the data and method used for the EFI, and present examples of EFI products.

2. Data and method

The EFI is a measure of the difference between the probability distribution of a real-time forecast and the climatological probability distribution (Lalaurette, 2003). It is a signed index with values ranging from -1 (all forecast members below the 0^{th} percentile of the climatology) to +1 (all forecast members above the 100^{th} percentile). We adopt a revised version of the EFI that adds weight to the tails of probability distributions (Zsótér, 2006).

The probability distribution of real-time forecasts is obtained from JMA one-month EPS values. The EPS consists of 25 members, and prediction is performed every Wednesday and Thursday. The reference climatological probability distribution (hereafter referred to as the model climate) is estimated based on five-member hindcasts (re-forecasts) starting on the nearest two initial dates during the period from 1981 to 2010. The initial dates of the hindcast are the 10^{th}, 20^{th} and last days of each month.

3. Examples of EFI products

In this section, we present examples of EFI products. First, Figure 1 shows a horizontal map of the EFI for the seven-day averaged temperature at 850 hPa based on EPS starting on October 27, 2011. The red (blue) regions indicate a high probability of extremely high (low) temperatures. As the EFI is a signed index, the probabilities of both high and low outliers can be summarized in one simple figure.

Second, Figure 2 shows an extreme weather warning map based on the EFI (Zsótér, 2006; Matsueda and Nakazawa, 2010). Here, extreme (abnormal) weather areas are defined as those where absolute EFI values exceed 0.8 (0.5). For example, areas where the EFI of temperature at 850 hPa exceeds 0.8 are identified as extremely warm. The product provides useful information for decision making by EPS users by combining multiple parameters.

The last product is the EFI meteogram (Figure 3) – a well-known meteorological product that displays time series representations of the EPS probability distribution and the EFI at individual points. Although the EFI's chief benefit is that it summarizes probability information simply in one index, it is also important for weather forecasters to directly understand the details of probability distributions. In this respect, the EFI meteogram is a supplement to the other two products.

4. Summary and future work

In this report, we have presented examples of the EFI-based products currently being developed by CPD/JMA. Future plans to improve the products include:

(1) Investigation of the relationship between the EFI and other indices for extreme weather forecasting (Nakazawa and Matsueda, 2010; Zsótér, 2006)

(2) Experimental use of the EFI in operational forecasting
(3) Verification of extreme event prediction based on the EFI

References

[1] Lalaurette, F., 2002: Early detection of abnormal weather conditions using a probabilistic extreme forecast index. *ECMWF Tech. Memorandum*, **373**.

[2] Lalaurette, F., 2003: Early detection of abnormal weather conditions using a probabilistic extreme forecast index. *Q. J. R. Meteorol. Soc.*, **129**. 3037–3057.

[3] Nakazawa, T. and M. Matsueda, 2010: Genesis potential estimation of high-impact weather by TIGGE ensemble data. *The 29th Conference on Hurricanes and Tropical Meteorology*, 15D.1.

[4] Zsótér, E., 2006: Recent developments in extreme weather forecasting. *ECMWF Newsletter* **107**, 8–17.

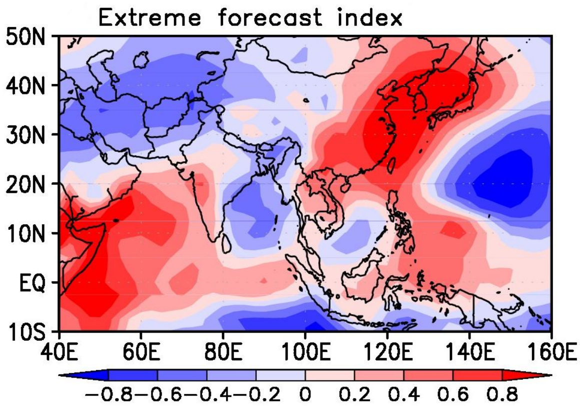

Figure 1. EFI map of temperature at 850 hPa from 1 to 7 November, 2011, obtained from JMA one-month prediction starting on 27 October, 2011. The red (blue) regions indicate a high probability of extremely high (low) temperatures.

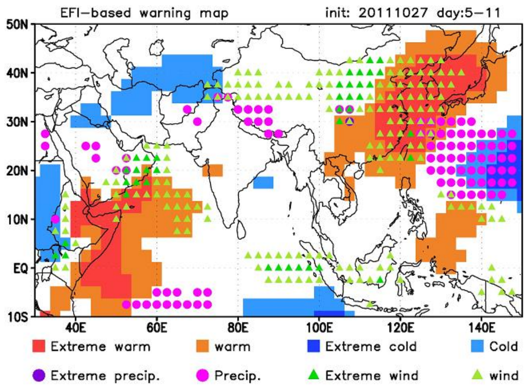

Figure 2. Extreme weather warning map based on EFI values. Extreme (abnormal) weather areas are defined as those where the absolute EFI value exceeds 0.8 (0.5). The period and the initial date of the forecast are the same as those for Fig. 1.

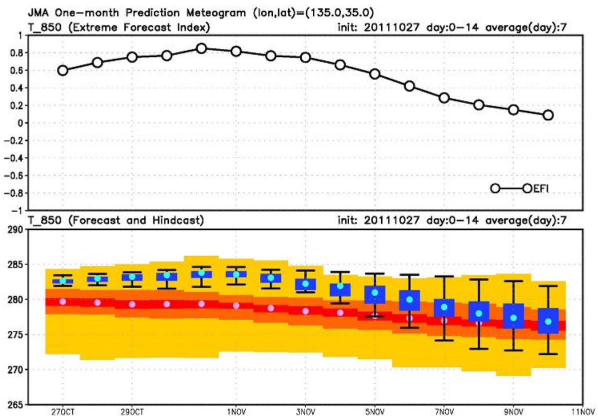

Figure 3. EFI meteogram for the seven-day averaged temperature at Kobe, Japan (135°E, 35°N). (top) Time series of EFI values. (bottom) Time series of the EPS forecast (cold color) and the model climate (warm color). The EPS forecast distribution is represented by box-whisker plots with the median (light-blue circles), the 20th/80th percentiles (blue boxes) and the minimum and maximum values (vertical lines). The model climate distribution is represented by box plots with the median (pink circles), the 10th/90th percentiles (red boxes), the 20th/80th percentiles (orange boxes) and the minimum and maximum values (yellow boxes).

Blockings Activity in the Northern Hemisphere: Tendencies of Change for Last Decades

Mokhov I.I.[1], Lupo A.R.[2], Prokofyeva M.A.[1]

[1]A.M. Obukhov Institute of Atmospheric Physics RAS, Moscow, Russia
[2]University of Missouri, Columbia, MO, USA
mokhov@ifaran.ru

During the most recent decades significant regional climate anomalies associated with atmospheric blocking anticyclones have been noted (Mokhov et al., 2011). According to (Mokhov et al., 1995; Mokhov and Petukhov, 1997) we have to expect the increase in characteristic life time τ_o for blocking anticyclones with the increase of surface temperature T from analysis of data for the Northern Hemisphere (NH) as a whole. With the use of exponential approximation $N=N_o exp(-\tau/\tau_o)$ for the number of blocking events N, and depending on their duration τ, it was estimated that $(\Delta\tau_o/\Delta T)/\tau_o$ = 0.13 K^{-1} from a comparison of the 10 warmest and 10 coldest years in the NH from the data for the period 1950-1990. Model simulations also display a similar tendency with more persistent blocking events for a warmer climate (Lupo et al., 1997).

Here we analyze data for the NH blocking events (with a minimum duration 5 days) from (http://solberg.snr.missouri.edu/gcc/) for the period 1969-2011 (see also (Wiedenmann et al., 2002)) together with the NH surface temperature data from (http://www.cru.uea.ac.uk/cru/data/temperature/). There is general agreement between the data for blockings used in (Mokhov and Petukhov, 1997) and the data analyzed here (Mokhov et al., 2001).

Figure 1 shows the number N of the NH blocking events depending on their duration τ (days) by data for all analyzed years. According to the linear regression lnN = -0.17τ + 1.15 (with coefficient of correlation r = 0.85) the characteristic time τ_o in the exponential model $N=N_o exp(-\tau/\tau_o)$ is equal to 5.9 days. The annual-mean number N_m, duration τ_m, and total duration $(N\tau)_m$ for the NH blocks during 1969-2011 were estimated to be equal to 27.7, 8.7, and 241.3 days, respectively.

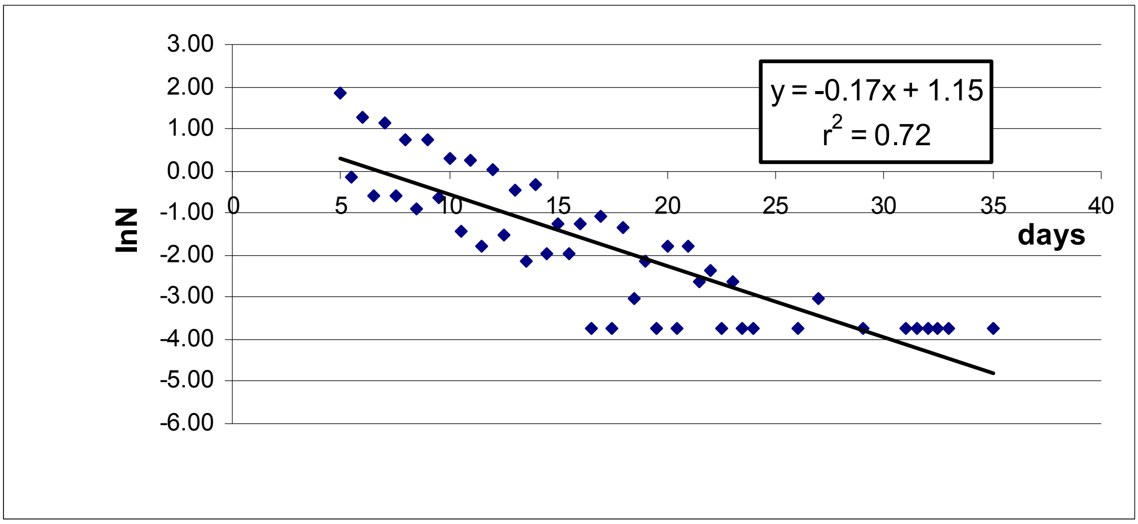

Fig. 1. Blocking numbers N depending on their duration τ (days) from the data for the Northern Hemisphere (1969-2011).

We compared also characteristics of blocking events for the 10 warmest years (1998, 2001-2007, 2009, 2010) and for the 10 coldest years (1969-1972, 1974-1976, 1978, 1984, 1985) in the Northern Hemisphere. The annual-mean number N_m of blocking events in the Northern Hemisphere for the 10 warmest years was estimated as 32.4, while for the 10 coldest years it was obtained equal to 26.6 (36% difference). The mean duration τ_m of blockings in the Northern Hemisphere for the 10 warmest years was equal to 9.8 days, while for the 10 coldest years it was estimated as 7.8 (23% difference). The total annual-mean duration $(N\tau)_m$ of blockings for the 10 warmest years was equal to 371.8 days, while for the 10 coldest years it was estimated as 206.8 days (57% difference). The characteristic time τ_o in the exponential approximation for blockings number N for the 10 warmest years was equal to 7.9 days, while for the 10 coldest years it was estimated as 5.5 (36% difference).

Similar to (Mokhov and Petukhov, 1997), it is possible to estimate the sensitivity of blockings characteristics to general warming with the use annual-mean difference in the NH temperature near surface ΔT between warm and cold decades (0.72 K). According to our estimates for a ΔT = 1 K the mean number of blocking events N_m, duration τ_m and total duration $(N\tau)_m$ are increasing on 49, 32% and 79%, respectively. The appropriate parameter of sensitivity $(\Delta\tau_o/\Delta T)/\tau_o$ = 0.50 K^{-1} for characteristic life time in the exponential approximation for the blocking number N corresponds to an increase in τ_o of 50% for ΔT = 1 K. This estimate is remarkably larger than that obtained by (Mokhov and Petukhov, 1997).

The characteristic time τ_o was estimated separately for blocking events persisting less than 20 days and for more persistent blockings. In the first case, τ_o was equal to 3.8 days. In the second case, the characteristic time τ_o was estimated to be three times larger (11.4 days).

This work was supported by the Russian Foundation for Basic Research, the programs of Russian Academy of Sciences and Russian Ministry of Education and Science.

References

Lupo A.R., R.J. Oglesby and I.I. Mokhov, 1997: Climatological features of blocking anticyclones: A study of Northern Hemisphere CCM1 model blocking events in present-day and double CO2 concentration atmospheres. Climate Dyn., **13**, 181–195.

Mokhov I.I., M.G. Akperov and A.A. Vetrova, 2011: Russian heat wave and blockings activity changes. Research Activities in Atmospheric and Oceanic Modelling, A. Zadra (ed.), Rep.41, S.7, 13-14.

Mokhov I.I. and V.K. Petukhov, 1997: Blockings and their tendencies of change. Doklady Earth Sci., **357**, 687-689.

Mokhov I.I., V.K. Petukhov, A.O. Senatorsky, 1995: Sensitivity of storm track activity and blockings to global climatic changes: Diagnostics and modeling. Publ. Acad. Finland. Painatuskaskus, **6/95**, 438-441.

Mokhov I.I., E.A. Tikhonova, A.R. Lupo, J.M. Wiedenmann, 2001: Atmospheric blocking characteristics in the Northern Hemisphere: Comparison of two climatologies. Research Activities in Atmospheric and Oceanic Modelling. Ed. by H. Ritchie. WMO/TD-No.1064, S.2, 20-21.

Wiedenmann J.M., A.R. Lupo, I.I. Mokhov and E.A. Tikhonova, 2002: The climatology of blocking anticyclones for the Northern and Southern Hemispheres: Block intensity as a diagnostic. J. Climate, **15**(23), 3459–3473.

Dynamics of Atmospheric Centers of Action

I.I. Mokhov, N.A. Nikitina
A.M. Obukhov Institute of Atmospheric Physics RAS, Moscow, Russia
mokhov@ifaran.ru

Interannual and long-term changes of atmospheric centers of action (ACAs) in the Northern (NH) and Southern (SH) Hemispheres were analyzed using different data sets based on reanalyses data and global climate model simulations with different CMIP5 scenarios (see also (Mokhov and Khon, 2005; Khon and Mokhov, 2006)). In particular, monthly-mean sea level pressure (SLP) data for different ACAs obtained from reanalyses ERA40 (period: 1957–2002; resolution: 2.5°x2.5°), ERA-Interim (1979–2011; 0.75°x0.75°), NCEP-NCAR(R1) (1948–2011; 2.5°x2.5°) and NOAA 20th-Century Reanalysis (Version 2) (1871-2010; 2°x2°) were analyzed. Also, we analyzed SLP simulations with different climatic general circulation models, including INM-CM4, IPSL (IPSL-CM5A-LR), HadCM3 with historical (1850-2005) and RCP scenarios (http://cmip-pcmdi.llnl.gov/cmip5/). Tendencies of change of ACAs were estimated with the use data from (http://www.cru.uea.ac.uk/cru/data/temperature/) for surface air and sea surface temperature.

Figure 1 shows interannual variations of the SLP anomalies (relative to corresponding means for the basic period 1961-1990) for the Siberian High in January based on different reanalyses data and climate model simulations. There is a large interannual variability for the Siberian High intensity. Nevertheless, Fig. 1 exhibites a general tendency of decrease in the Siberian High intensity (SLP at its center) under warming in the 21st century with RCP anthropogenic scenarios. This decrease is faster for the RCP 8.5 scenario than that for the RCP 4.5 scenario.

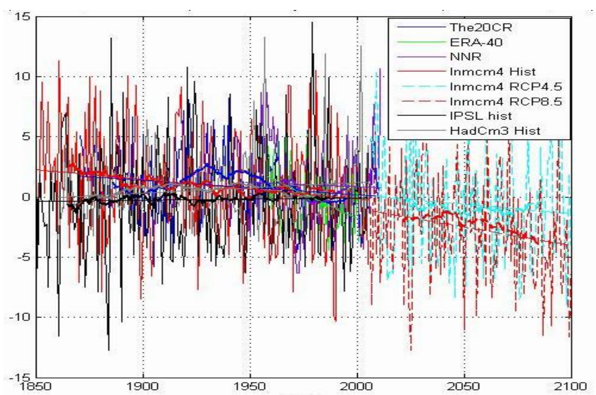

Fig. 1. SLP anomalies (hPa) at the center of the Siberian High in January obtained from various reanalyses data and global climate model simulations for the 19th-21st centuries.

Remarkable variations were also noted for other ACAs, in particular for the Aleutian Low in winter.

The relationship of the ACA characteristics with climate changes can be revealed with the use of cross-wavelet analysis (see (Jevrejeva et al., 2003)). Figure 2 shows local coherency between the intensity of Siberian High from the NOAA 20th-Century Reanalysis (Version 2) data and NH surface temperature in March. It was exhibited significant interdecadal and longer-term coherency in the second half of the 20th century and at the beginning of the 21st century, especially during early spring (March) and late fall (November).

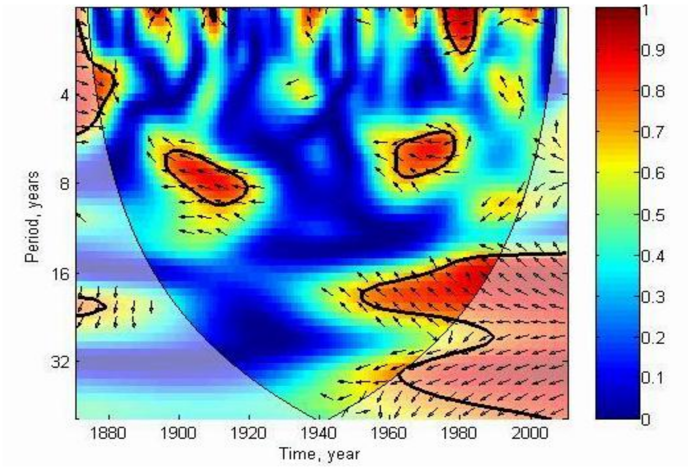

Fig. 2. Local coherency between the intensity of Siberian High and NH surface temperature in March.

Cross-wavelet analysis reveals also relationships between different ACAs. In particular, significant coherency was exhibited for long-term variations of polar ACAs. Figure 3 shows local coherency between the Arctic and Antarctic High intensities in January obtained from the NOAA 20th-Century Reanalysis (Version 2) data.

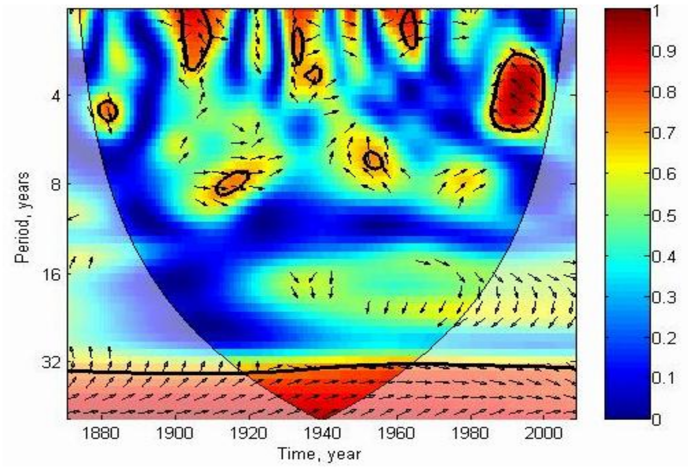

Fig. 3. Local coherency between the Arctic and Antarctic High intensities in January.

This work was supported by the Russian Foundation for Basic Research, the programs of Russian Academy of Sciences and Russian Ministry of Education and Science.

References

Jevrejeva S., Moore J.C., Grinsted A., 2003: Influence of the Arctic Oscillation and El Nino-Southern Oscillation (ENSO) on ice condition in the Baltic Sea: The wavelet approach. *J. Geophys. Res*., **108**(D21), 4677, doi:10.1029/2003JD003417.

Khon V.C., and I.I. Mokhov, 2006: Model estimates for the sensitivity of atmospheric centers of action. *Izvestiya, Atmos. Ocean. Phys.*, **42**, 688-695.

Mokhov I.I. and V.C. Khon, 2005: Interannual variability and long-term tendencies of change in atmospheric centers of action in the Northern Hemisphere: Analyses of observational data. *Izvestiya, Atmos. Ocean. Phys.*, **41**, 657-666.

REANALYSIS DATA VALIDATION USING THE ANNUAL VARIATION OF DAILY CLIMATIC CHARACTERISTICS AS COMPARED TO STATION OBSERVATIONS

A.Muraviev, I.Kulikova
Hydrometeorological Research Centre of the Russian Federation
Bol. Predtechensky per., 11-13, 123242 Moscow, Russia
muravev@mecom.ru, kulikova@mecom.ru

Seasonal hydrodynamic ensemble forecasting, performed at the North Eurasia Climate Center (NEACC, Moscow) with perspective of weekly issuance, should use daily resolved climatic values in observations, model hindcasts, as well as in "reference" reanalysis archives [3].

For comparing the annual variation of daily surface air temperature norms and standard deviations over the Eurasian territory of the former USSR, we applied station observations [1] and the nearest point data of the NSEP-NCAR reanalysis grid [2]. Characteristics were calculated over the 1979-2008 period with special attention to stations representative for six main climatic regions of the FU.

Figure 1 demonstrates a substantial discrepancy in daily normals (a) *in winter time*, e.g. for *Moscow* with a temperate climate the reanalysis yields 1°-2°C lower temperatures, and (b) *in Central Asia*, e.g. the reanalysis underestimates 8°-10°C for *Tashkent* through the whole year. The reanalysis annual amplitude in some regions with sharp-continental climate (*Verchoyansk*) is diminished, whereas in other regions with similar climate conditions (*Kustanay*, Northern Kazakhstan) the agreement is quite satisfactory. The two curves also coincide for the monsoon region of the Far East (*Khabarovsk*).

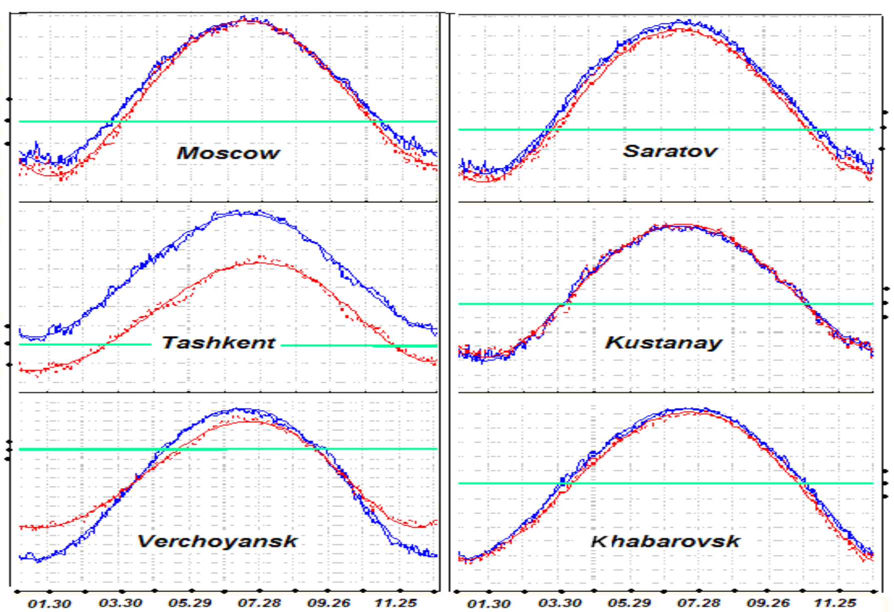

Figure1. Annual variation of daily surface air temperature normals at stations (blue) and at nearest reanalysis points (red). Points at the vertical coordinates indicate 4°C intervals around the zero value (green line). The date coordinate depicts 30 days intervals. Curves are approximated by the 5th order polynomial.

Figure 2 demonstrates the annual variation of daily standard deviation from the sample norms calculated over the given period. Significant similarity in global extremes is obvious revealing minimum variability in summer and maximum variability in winter. However the amplitude diversity during the year is also remarkable (*Verchoyansk*).

Another prominent feature should be noted. The majority of stations in the European part of Russia up to the Urals reveal a second local maximum by the end of spring (e.g. Figure 2, *Ekaterinburg*), which can be interpreted as climatic 'spring cold wave' due to the so called 'ultra-polar air intrusions'. This feature is either absent or insignificant to the east of the Urals. These local maxima can usually be found in reanalysis data verifying to some extent their climatological character.

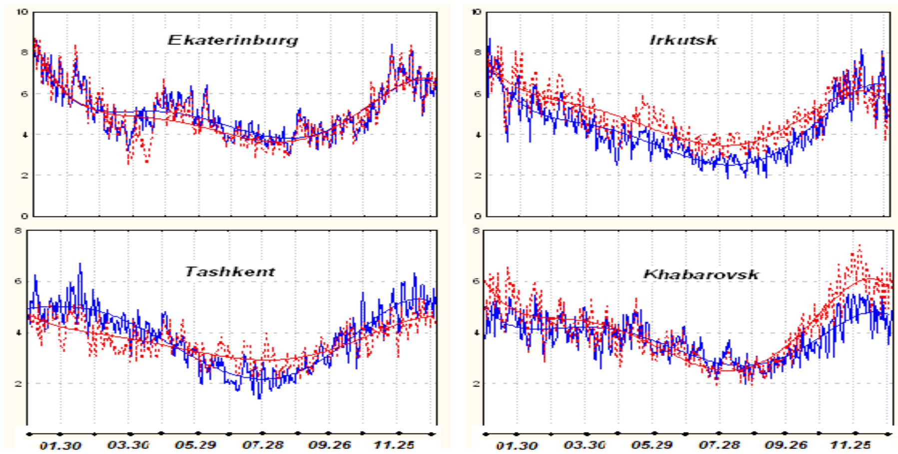

Figure 2. Annual variation of daily surface air temperature deviations at stations (blue line) and at nearest reanalysis grid points (red line). Curves are approximated by the 5th order polynomials.

Figure 3 shows spectral filtering of the annual variation of daily surface air temperature deviations at station *Moscow*. Three Fourier components (Fig.3, S07 in legend) are quite sufficient for the filter to 'pass' this local variability maximum. The question still remains: which local extreme is 'climatic', and which should be filtered as 'non-climatic noise'?

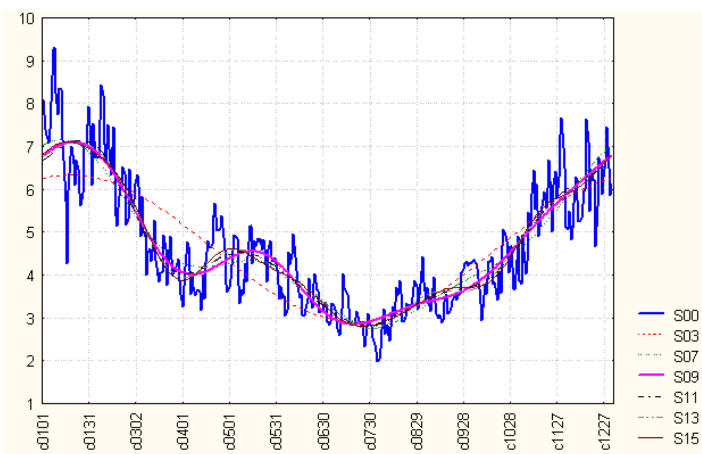

Figure 3. Annual variation of daily surface air temperature deviations at station Moscow (blue line). The initial series is approximated by increasing number of the Fourier components. The legend shows numbers equaling doubled component number plus one.

1. VNIIGMI-archive, Russian Inst. for Hydrometeorological Information, 2007: http://meteo.ru/english/.
2. Kanamitsu, M., and Coauthors, 2002. NCEP–DOE AMIP-II Reanalysis (R-2) // Bull. Amer. Met. Soc., **83**, 11, p.1631–1643.
3. Schemm, J-K., and Coauthors., 1998: Construction of daily climatology based on the 17-year NCEP-NCAR reanalysis. Proc. of the 1st WCRP Intern. Conf. on Reanalyses. Silver Spring, Maryland, USA. 290-293.

The Concordiasi field experiment over Antarctica: first results from innovative atmospheric measurements

Florence Rabier[1], Steve Cohn[2], Philippe Cocquerez[3], Albert Hertzog[4], Linnea Avallone[5], Terry Deshler[6], Jennifer Haase[7], Terry Hock[2], Alexis Doerenbecher[1], Junhong Wang[2], Vincent Guidard[1], Jean-Noël Thépaut[8], Rolf Langland[9], Andrew Tangborn[10], Gianpaolo Balsamo[8], Eric Brun[1], David Parsons[11], Jérôme Bordereau[4], Carla Cardinali[8], François Danis[4], Jean-Pierre Escarnot[3], Nadia Fourrié[1], Ron Gelaro[10], Christophe Genthon[12], Kayo Ide[13], Lars Kalnajs[5], Charlie Martin[2], Louis-François Meunier[1], Jean-Marc Nicot[3], Tuuli Perttula[14], Nicholas Potts[2], Patrick Ragazzo[3], David Richardson[8], Sergio Sosa-Sesma[3], André Vargas[3]

1 CNRM-GAME, Météo-France and CNRS; 2 NCAR/EOL; 3 Centre National d'Etudes Spatiales; 4 Laboratoire de Météorologie Dynamique; 5 University of Colorado; 6 University of Wyoming; 7 Purdue University; 8 European Centre for Medium range Weather Forecasts; 9 Naval Research Laboratory; 10 Global Modeling and Assimilation Office; 11 Ohio University; 12 Laboratoire de Glaciologie et Géophysique de l'Environnement; 13 University of Maryland; 14 Finnish Meteorological Institute

Concordiasi field campaign

Concordiasi is a multi-disciplinary effort studying the lower stratosphere, troposphere, and land surface of Antarctica. In 2010 an innovative constellation of balloons provided a unique set of measurements covering both volume and time. The balloons drifted for several months on isopycnic surfaces in the lowermost stratosphere around 18km, circling over Antarctica in the winter vortex. In situ measurements included position, temperature, pressure, ozone, and particles, and profiles below the gondolas included temperature, pressure, humidity, and winds. Nineteen balloons were launched, between September 8th and October 26th. The mean flight duration was 69 days.

Stratospheric balloons, gravity-waves and GPS/Radio Occultation measurements

In-situ balloon-borne meteorological observations are first useful to study the activity of mesoscale gravity waves above Antarctica and the surrounding oceans. Due to the quasi-Lagrangian behavior of long-duration balloons, the gravity-wave intrinsic frequencies and momentum fluxes can be directly inferred from these observations. During Concordiasi, these observations were made every 30s, so as to resolve the whole spectrum of gravity waves. First analyses indicate the signature of mountain waves above the Antarctic Peninsula, and significant activity above the ocean. A proof-of-concept balloon-borne GPS radio occultation system was furthermore deployed on two of the Concordiasi campaign balloon flights to provide refractivity and derived temperature profiles for validation and improving satellite data assimilation. 711 occultations were recorded, comparable to the total number of dropsonde profiles.

Ozone and Particle observations

The in-situ observations of temperature, ozone, and particle size from the Concordiasi balloons provided new observations, along near Lagrangian trajectories, of the evolution of ozone and particle size as the sun returned to the Antarctic stratosphere. The instruments were designed to take advantage of this unique opportunity to observe, along air parcel paths, changes in ozone due to photochemical destruction, and changes in particle size due to temperature changes. The ozone measurements were made on six balloons, four of which were launched in early September. The Concordiasi payloads provided unique observations of ozone from which near-instantaneous ozone loss rates can be determined. Initial calculations suggest that ozone is being lost at rates up to 10 ppb per sunlit hour, which is slightly larger than published values.

Driftsonde data

The needs of Concordiasi spurred technological advances of the NCAR Driftsonde system, which provided unprecedented high-quality, high vertical resolution upper air observations from float level to the surface. Overall, the 13 Driftsonde gondolas returned 644 high quality profiles. Consistent cold biases are found in all satellite data except in the upper troposphere in Microwave Integrated Retrieval System (MIRS) and in the lower troposphere in the Infrared Atmospheric Sounding Interferometer (IASI). The cold bias is larger relative to dropsondes than radiosondes as a result of a larger cold bias over the Antarctic continent than the coast and ocean. All radiosonde stations but a couple are located along the coast. The satellite data can reproduce observed temperature profiles reasonably well in spite of the biases.

Impact of the data in NWP models in the Southern polar area

Concordiasi meteorological observations, both at the gondola level and from the dropsondes were used in real-time at Numerical Weather Prediction Centres. The comparison between short-range forecasts and the data was investigated for 7 centres in the US, France, Canada, ECMWF, Japan, Germany and the United-Kingdom. Results show that models suffer from deficiencies in representing near-surface temperature over the Antarctic high terrain. The very strong thermal inversion observed in the data is a challenge in numerical modelling, because models need both a very good representation of turbulent exchanges in the atmosphere and of snow processes to be able to simulate this extreme atmospheric behaviour. Dropsondes were shown to have a positive impact on the forecast performance in four different models, with an impact of the same order of magnitude as the one brought by radiosondes. The total short-range forecast error-reduction produced by assimilation of dropsonde observations from Concordiasi is smaller than that provided by satellite radiance and wind observations, although the average error reduction per-observation is much larger for dropsondes compared to satellite data. For the dropsonde observations, both temperature and wind data have more impact when they are closer to the pole, with temperature information contributing most at low levels while wind information dominates at high levels (<400 hPa). On a per-observation basis, however, both wind and temperature have larger impact closer to the surface (lower troposphere). This corresponds to areas where there are very few other competing observations, mainly because of the difficulty of using satellite radiance information close to the surface, especially over high terrain.
The development of a Lagrangian approach to assimilating the driftsonde positions into the GEOS5 assimilation system at NASA's Global Modeling and Assimilation office has been developed. Lagrangian assimilation utilizes position observations by producing a forecast of the balloon positions through a forward model of the balloon trajectory. The correction to the wind fields is done through the tangent linear and adjoint of this model. Initial testing of the Lagrangian assimilation in 3DVAR mode showed that it is essentially equivalent to assimilating derived winds from the balloons.

Interactions of the lower atmosphere with the snow over Antarctica

At the surface, particular attention has been paid to the observation and the modeling of the interaction between snow and the atmosphere, which controls surface and near-surface temperatures and strongly influences the radiances as measured by the IASI satellite-borne sensor. The Dome-C Concordia station has been the focal point of this activity, thanks to its exceptional instrumentation, including observations of atmospheric profiles with a 45 m tower, turbulence, radiation, and snow-profile, among others. Both NWP operational and research models have been evaluated. This research has led to an improvement of snow representation over Antarctica in the IFS model at ECMWF. Coupled snow-atmosphere simulations performed at Météo-France with the Crocus/AROME models have been shown to realistically reproduce the snow internal and surface temperatures and boundary layer characteristics.

Website: http://www.cnrm.meteo.fr/concordiasi/
Data can be accessed at the following address http://www.cnrm.meteo.fr/concordiasi-dataset/

Arctic warming and the trend from snowfall to rain

James A. Screen and Ian Simmonds

School of Earth Sciences, The University of Melbourne, Victoria, 3010, Australia
screenj@unimelb.edu.au

We are exploring some of the mechanisms responsible for 'Arctic amplification' of the global warming signal (Arctic warming is observed in all months (Screen and Simmonds 2010).) One of this is potentially associated with a warmer polar environment more likely to produce rainfall rather than snow. In such a scenario, the surface albedo decreases and encourages more absorption of solar radiation.

To investigate this we have made use of the ERA-Interim reanalyses for the 1989-2009 period. The proportion of precipitation occurring as snow can be expressed by the snowfall-to-precipitation ratio (SPR); i.e.,

$$SPR = \frac{S_{we}}{P}$$

where S_{we} is the daily total snowfall water equivalent (mm-we day^{-1}) and P is the daily total precipitation (mm day^{-1}). Days with no precipitation are not considered. We calculate the Arctic-mean SPR as:

$$SPR_{arctic} = \frac{\overline{S_{we}}}{\overline{P}}$$

where the overbar denotes the area-average north of 70°N.

Fig. 1 which shows the mean annual cycles of SPR and surface temperature averaged over the Arctic. We have calculated the ERA-Interim Arctic-mean trends in these precipitation quantities (Fig. 2). The largest seasonal-mean Arctic-mean changes in SPR are in summer, when the proportion of precipitation falling as snow has significantly decreased. A smaller, but still statistically significant, decrease in SPR is depicted in autumn. However, these two seasons show contrasting changes in snowfall and total precipitation. In summer, there has been a decrease in snowfall and total precipitation. The decline of snowfall exceeds the total precipitation decrease resulting in the decrease in SPR. Given that the majority of precipitation in summer falls as rain one would expect a decrease in total precipitation to be associated with a decrease in rainfall. That rainfall has increased and not decreased, when the total precipitation has decreased, reflects the decrease in the SPR. Had SPR remained constant, rainfall would have decreased in line with decreasing precipitation. In autumn, there is a large increase in total precipitation and only a small increase in snowfall. This increase in snowfall cannot be related to changes in precipitation form as SPR has decreased and must be related to the increase in total precipitation. This additional precipitation has disproportionately fallen as rain rather than snow, as reflected by the decrease in SPR and the large increase in rainfall.

Further details may be found in Screen and Simmonds (2012).

Screen, J. A., and I. Simmonds, 2010: Increasing fall-winter energy loss from the Arctic Ocean and its role in Arctic temperature amplification. *Geophys. Res. Lett.*, **37**, L16707, doi:10.1029/2010GL044136.

Screen, J. A., and I. Simmonds, 2012: Declining summer snowfall in the Arctic: Causes, impacts and feedbacks. *Climate Dyn.*, doi: 10.1007/s00382-011-1105-2.

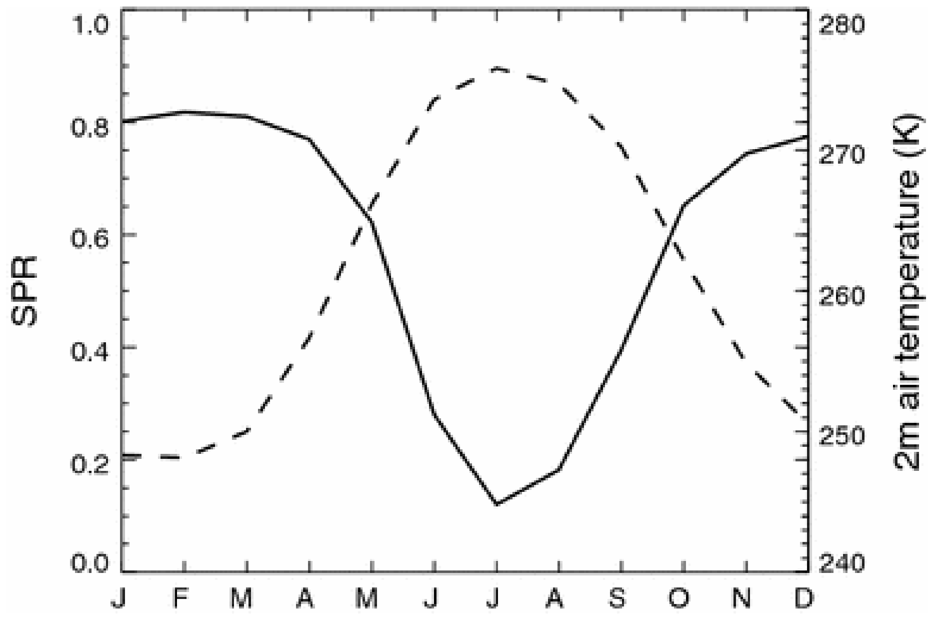

Figure 1: Monthly climatologies of the Arctic-mean (north of 70°N) SPR (*solid*) and surface air temperature (*dashed*) in ERA-Interim, 1989-2009

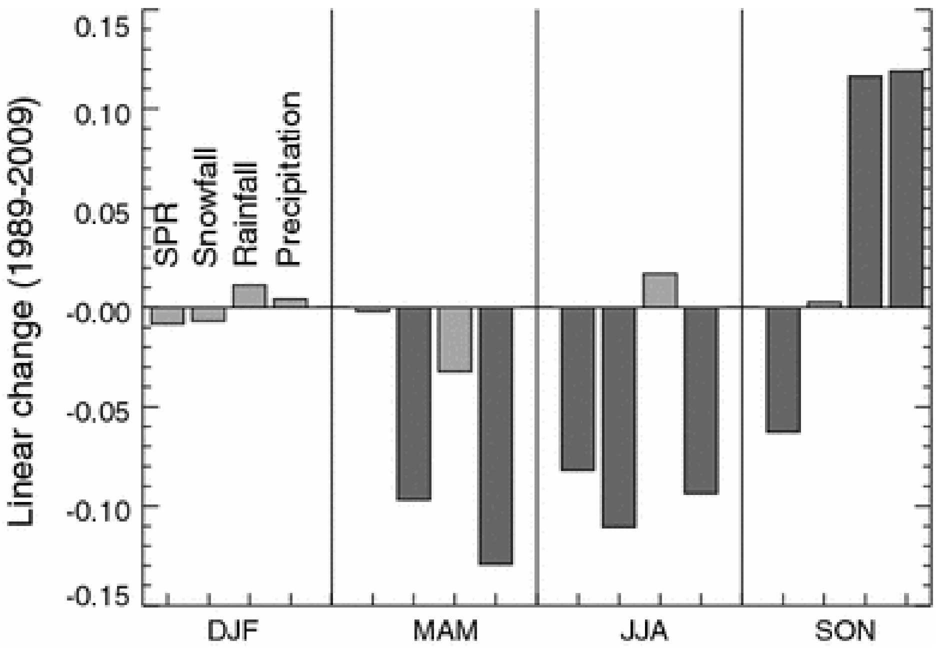

Figure 2: Linear changes from 1989 to 2009 in seasonal-mean Arctic-mean SPR, daily snowfall (mm-we day^{-1}), daily rainfall (mm day^{-1}) and daily total precipitation (mm day^{-1}) in ERA-Interim. *Darker bars* denote linear changes that are statistically significant ($p < 0.10$).

WGNE Intercomparison of Tropical Cyclone Track Forecasts from Operational Global Models and Regional Models

Akira SHIMOKOBE*, Hironori UMEZU and Satoshi MORIYASU
Numerical Prediction Division, Japan Meteorological Agency
Email: shimokobe@met.kishou.go.jp

1. Introduction

Since 1991, the CAS/JSC Working Group on Numerical Experimentation (WGNE) has conducted intercomparison of tropical cyclone track forecasts using operational global models. This time is the 20th aniversary. In 2010, the project involved eleven such models, and verification of six regional models was also conducted for the first time.

2. Datasets and verification method

Table 1 shows the specification of global models datasets provided by participating NWP centers, and Table 2 shows the corresponding information for regional models.

The verification area is divided into six regions according to the domains of responsibility for each TC RSMC. Best-track data provided by each RSMC is used in the verification. The verification method of Sakai and Yamaguchi (2005) was adopted in this study.

Table 1 Global model specifications

NWP centers	Participate Year	Bogus data	Model Res. as of 2010
BoM	2003	-	80kmL50
CMA	2004	used	T$_L$639L60
CMC	1994	-	0.45° x0.3° L58
DWD	2000	-	40kmL40(- Feb.) 30kmL40(Feb.-)
ECMWF	1991	-	T$_L$799L91(-Jan.) T$_L$1279L91(Jan.-)
JMA	1991	used in WNP	T$_L$959L60
KMA	2010	used	T426L40(-May.) 40kmL50（May.-）
France	2004	usedexcept for South Pacific and north Indian-Ocean	T538C2.4L70(-Apr.) T$_L$798C2.4L70(Apr.-)
NCEP	2003	used in rare case	T382L64(-Jul.) T574 L64 (Jul.-)
NRL	2006	used	T239L30
UKMO	1991	used	40kmL70(-Mar.) 25kmL70(Mar.-)

Table 2 Regional model specifications

NWP centers	Name of Model	Verification Region	Bogus data	Model Res. as of 2010
JMA	MSM	WNP	Used	5kmL50
KMA	Unified Model	WNP (north to 20N west to 140E)	Used	12kmL38
France	Aladin-Reunion	SIO (31E-88.5E 32S-0)	Used	8kmL70
NCEP	HWRF	NAT,ENP	Used	inner 9km outer 27km L42
	GFDL	NAT,ENP	Used	1/12 degree(third nest) L42
UKMO	South Asia Regional Model	NIO	Not Used	12kmL70

3. Global model verification

Figure 1 shows the position error growth for the global models over the western North Pacific and North Atlantic regions. The error of the ECMWF forecast is very small during the verification period over the western North Pacific. On the whole, the error growth for the North Atlantic is smaller than that for the western North Pacific. Figure 2 shows the position error of operational models in these 20 years. It can be seen that tropical cyclone track forecasting has gradually improved at all operational centers along with the enhancements to their NWP systems.

4. Regional model verification

Figure 3 shows the position error growth for regional models, with thick lines indicating the errors for each one. It can be seen that most are better at forecasting TC tracks than the global models of their respective countries.

References

Sakai, R. and M. Yamaguchi, 2005: The WGNE Intercomparison of Tropical Cyclone Track Forecasts by Operational Global Models. CAS/JSC WGNE Research Activities in Atmospheric and Oceanic Modeling, Report No. 35, Jul. 2005, 2.7 –2.8.

Onoda, H. and T. Komori, 2009: WGNE Intercomparison of Tropical Cyclone Forecasts using Operational Global Models. CAS/JSC WGNE Research Activities in Atmospheric and Oceanic Modeling, Report No. 39, Oct. 2009, 2.21 –2.22.

Muroi, C. and N. Sato, 1994: Intercomparison of tropical cyclone track forecast by ECMWF, UKMO and JMA operational global models, Japan Meteorological Agency JMA/NPD Technical Report No. 31, 26pp.

Tsuyuki, T., R. Sakai and H. Mino, 2002: The WGNE intercomparison of typhoon track forecasts from operational global models for 1991-2000. WMO-BULLETIN, Vol. 5, No. 3, 253 –257.

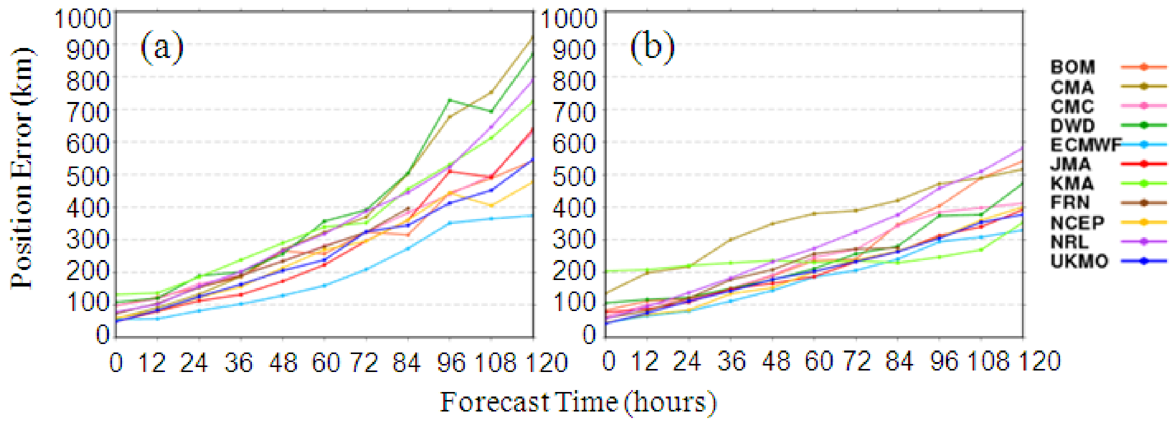

Fig.1 Position error growth in (a) the western North Pacific, and (b) the North Atlantic

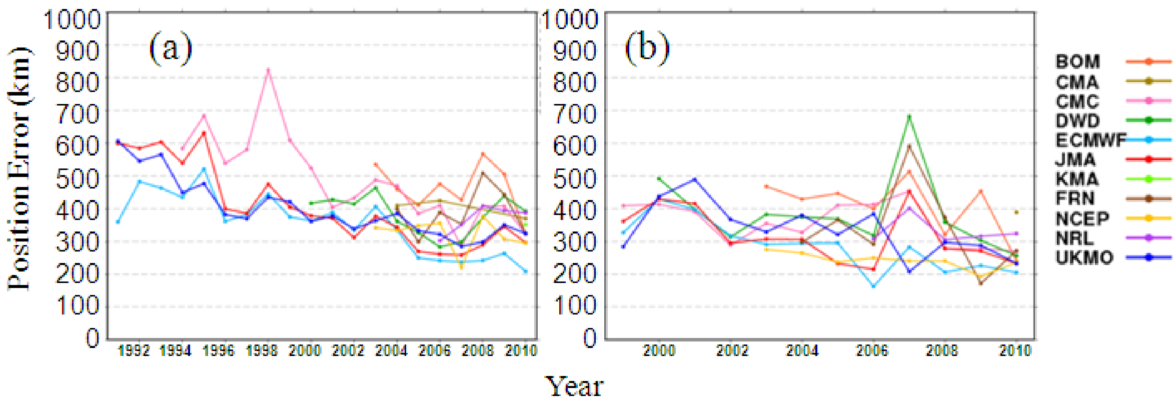

Fig.2 Transition of 72-hour forecast position errors over (a) these 20-year period starting in 1991 for the western North Pacific, and (b) these 12-year period starting in 1999 for the North Atlantic

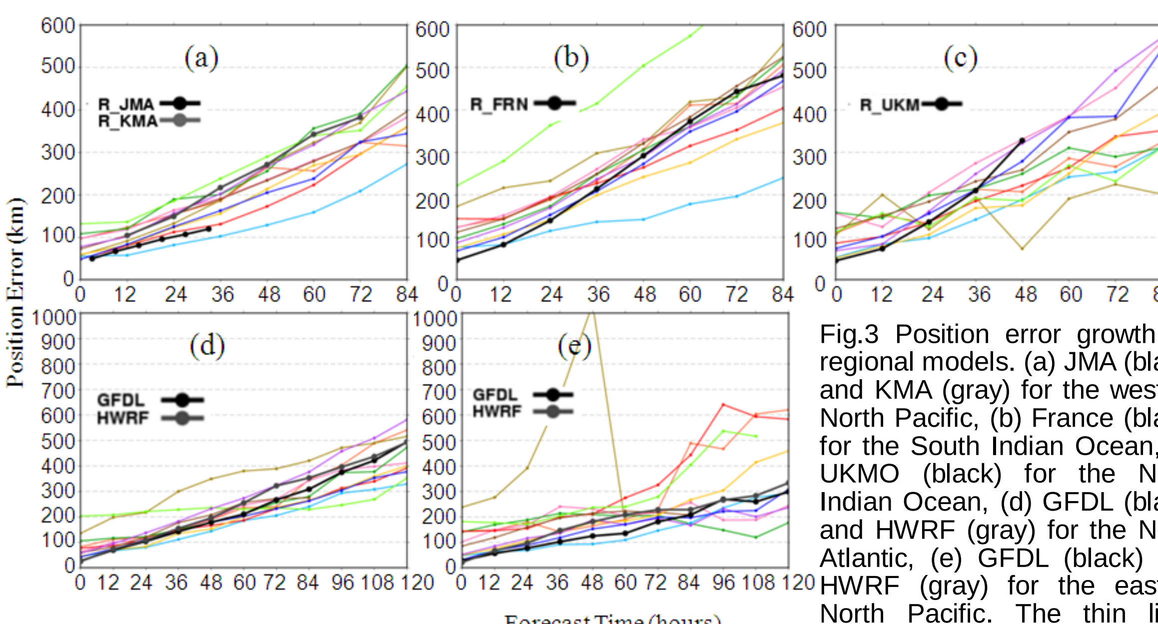

Fig.3 Position error growth for regional models. (a) JMA (black) and KMA (gray) for the western North Pacific, (b) France (black) for the South Indian Ocean, (c) UKMO (black) for the North Indian Ocean, (d) GFDL (black) and HWRF (gray) for the North Atlantic, (e) GFDL (black) and HWRF (gray) for the eastern North Pacific. The thin lines show the error growth from the global models. The line colors are the same as those for Figs. 1 and 2.

Trends in the behaviour of 850 hPa fronts in the southern extratropics

Ian Simmonds

School of Earth Sciences, The University of Melbourne, Victoria, 3010, Australia
simmonds@unimelb.edu.au

There has been much research in recent times exploring the trends in extratropical cyclone behaviour in the SH (e.g., Simmonds and Keay 2000, Irving et al. 2010). However, very little attention has been paid to the more challenging task of diagnosing trends in frontal behaviour over the southern extratropics.

We report on some preliminary investigations into changes in frontal frequency, and well as trends in the length and intensity of fronts. The frontal identification and tracking package we have used here is that described by Simmonds et al. (2012). The scheme is applied at the 850 hPa level of the ERA–Interim reanalysis (Dee et al. 2011) over the 20-year period 1989-2008.

The top panel of Figure 1 shows the trends in the annual frequency distribution of the centroids of all identified frontal structures. Significant reductions in frontal numbers are diagnosed in the Southern Ocean to the south of Australia and new Zealand. By contrast the western Indian at about 50°S hosts an increase in frontal frequency. The middle panel of Figure 1 shows very little change in mean frontal length over our relatively short period of our analysis. By contrast the significant trends in mean frontal intensity (bottom panel of Figure 1) are predominantly positive, with notable increases in intensity in the Tasman Sea, to the southwest of Australia, and in the eastern Pacific at about 40°S.

Dee, D. P., et al., 2011: The ERA-Interim reanalysis: Configuration and performance of the data assimilation system. *Quart. J. Roy. Meteor. Soc.*, **137,** 553-597.
Irving, D., I. Simmonds and K. Keay, 2010: Mesoscale cyclone activity over the ice-free Southern Ocean: 1999-2008. *J. Climate,* **23,** 5404–5420.
Simmonds, I., and K. Keay, 2000: Variability of Southern Hemisphere extratropical cyclone behavior 1958-97. *J. Climate,* **13,** 550-561.
Simmonds, I., K. Keay and J. A. T. Bye, 2012: Identification and climatology of Southern Hemisphere mobile fronts in a modern reanalysis. *J. Climate,* **25,** 1945-1962.

Figure 1 (next page): Annual mean trends (per decade) of 850 hPa frontal characteristics over 1989-2008. (top) frequency of frontal centroid positions, (middle) length, and (bottom) intensity. The units are counts per 10^3 (degrees of latitude)^2, km, and ms^{-1} (1000 km), respectively. Stippling denotes where trends are significantly different from zero ($p < 0.05$).

ERAIN 850hPa PM-LC SH ANN 1989 SD Fix b values

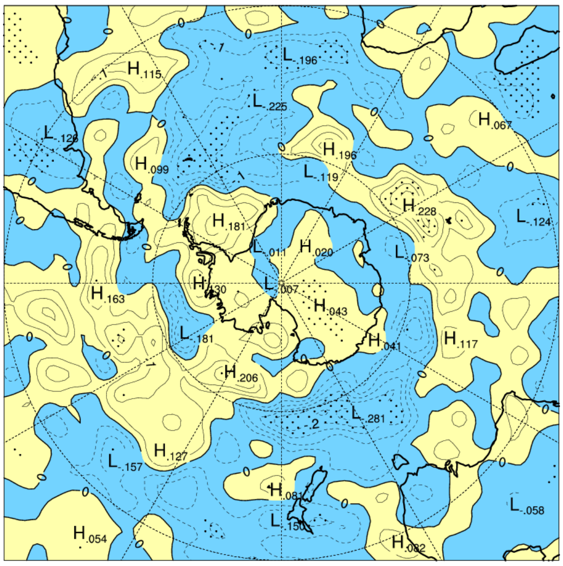

CONTOUR FROM -.25 TO .2 BY .05

ERAIN 850hPa PM-LC SH ANN 1989 L Fix b values

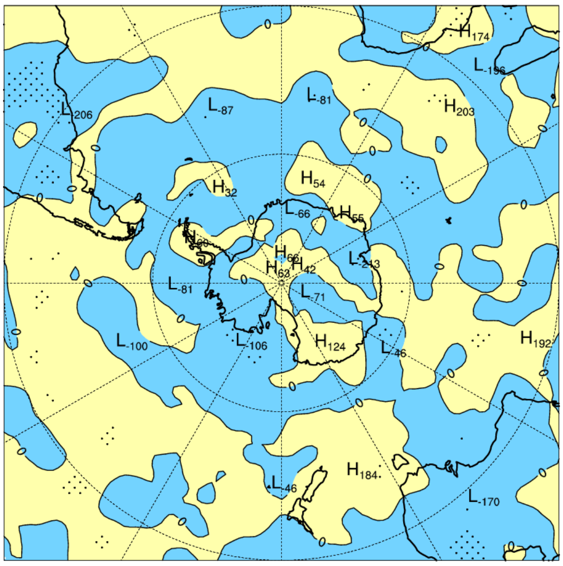

CONTOUR FROM -800 TO 600 BY 200

ERAIN 850hPa PM-LC SH ANN 1989 I Fix b values

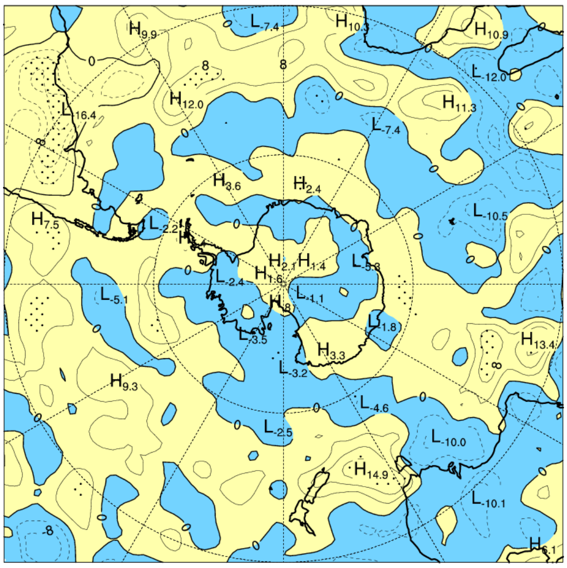

CONTOUR FROM -16 TO 12 BY 4

Southern Ocean atmospheric fronts identified in ERA-Interim

Ian Simmonds, Kevin Keay, and John A. T. Bye

School of Earth Sciences, The University of Melbourne, Victoria, 3010, Australia
simmonds@unimelb.edu.au

Our group has for many years developed algorithms for the automatic detection and tracking of cyclones in global analyses (e.g., Simmonds and Keay 2002, Lim and Simmonds 2007) This work has now been extended to the tracking of atmospheric fronts. Such features are central components of weather (and hence climate) over much of the world.

Simply described, our mobile frontal identification determines all points at which between successive 6-hourly analyses (i) the 10m wind changes from the northwest quadrant to the southwest quadrant and (ii) the arithmetic value of the change in the meridional wind exceeds $2ms^{-1}$. As described in detail by Simmonds et al. (2012) we compile all such points into 'frontal objects', and locate fronts at the eastern edge of these objects. We determine a range of statistics from each front so-identified, including the centroid of its frontal points, the length of the front, and its 'intensity' (defined as the meridional wind change integrated along the length of the front).

We apply our scheme to the identification of surface (10m) fronts over the southern extratropics to the ERA–Interim reanalysis (Dee et al. 2011) for all winters (JJA) over the 20-year period 1989-2008.The top panel of Figure 1 shows the frequency distribution of all frontal points, with high values cantered near 50ºS in the Indian Ocean . The distribution of frontal length (the length of each front being plotted at the centroid of its frontal points) also shows its maximum values in the Indian Ocean (close to 2,000 km), and secondary maximum in the Atlantic Ocean (middle panel). The bottom panel in Figure 1 presents the winter mean of the intensity (again plotted at the centroid of each individual front); this also shows its extreme values to the south and upstream of Australia. The mean intensity of fronts in the Pacific Ocean is relatively low.

Dee, D. P., et al., 2011: The ERA-Interim reanalysis: Configuration and performance of the data assimilation system. *Quart. J. Roy. Meteor. Soc.*, **137,** 553-597.

Lim, E.-P., and I. Simmonds, 2007: Southern Hemisphere winter extratropical cyclone characteristics and vertical organization observed with the ERA-40 reanalysis data in 1979-2001. *J. Climate*, **20,** 2675-2690.

Simmonds, I., and K. Keay, 2002: Surface fluxes of momentum and mechanical energy over the North Pacific and North Atlantic Oceans. *Meteor. Atmos. Phys.*, **80,** 1-18.

Simmonds, I., K. Keay and J. A. T. Bye, 2012: Identification and climatology of Southern Hemisphere mobile fronts in a modern reanalysis. *J. Climate,* **25,** 1945-1962.

Figure 1 (next page): JJA climatology of the characteristics surface fronts. (top) frequency, (middle) length, and (bottom) intensity. The units are counts per 10^3 (degrees of latitude)^2, km, and ms^{-1} (1000 km), respectively.

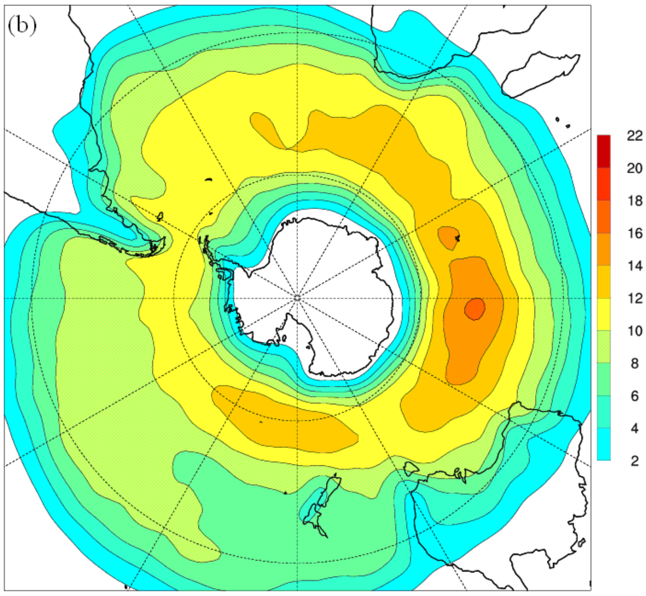
(b)
22
20
18
16
14
12
10
8
6
4
2

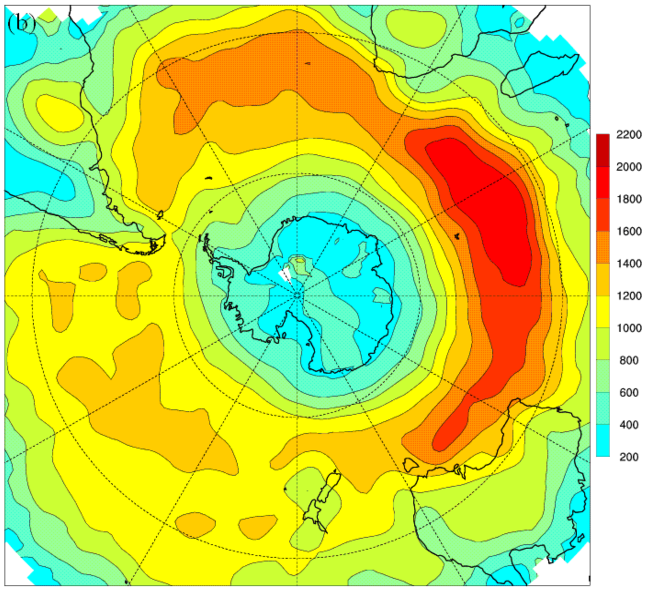
(b)
2200
2000
1800
1600
1400
1200
1000
800
600
400
200

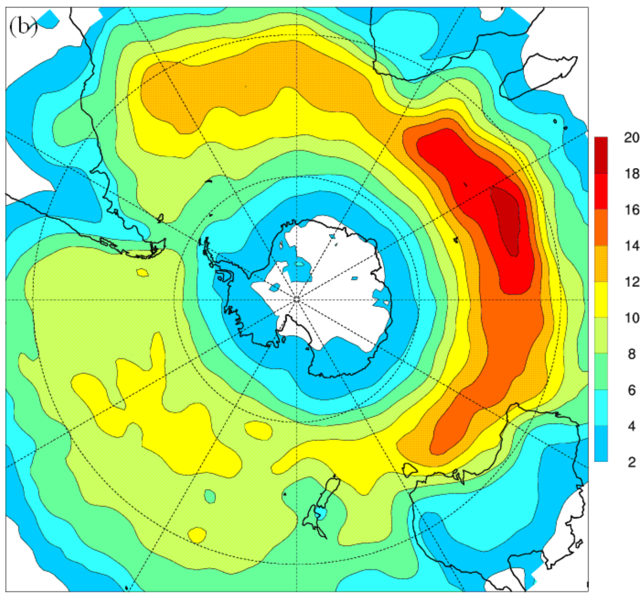
(b)
20
18
16
14
12
10
8
6
4
2

A Study of Quasi-millennial Extratropical Cyclone Activity Using Tracking and Clustering Methods

Lan Xia, Hans von Storch, Frauke Feser
Institute of Coastal Research, Helmholtz-Zentrum Geesthacht, Geesthacht, Germany

1. Overview

Northern Hemispheric extratropical storm tracks are determined in mean sea level pressure fields (MSLP) of a quasi-millennial (1001-1990) global climate simulation by ECHO_G using a previously developed tracking algorithm (Hodges 1999). The ECHO-G simulation was shown skillful in simulating the seasonal mean climatology and inter-annual variability of MSLP (Gouirand et al. 2007). The numbers of tracks from the ECHO-G simulation data are on a similar level as those derived from the NCEP/NCAR reanalysis data. Winter storm tracks of the northern hemisphere (NH) are clustered in ten groups using the k-means clustering method. Climatological changes of extratropical cyclones in winter including frequency, density and lifespan are analyzed for each group.

2. Results

The cyclones are detected and tracked by the tracking algorithm of Hodges (1999). It detects the minima on the MSLP fields and connects the minima to form tracks. Minimum lifetimes of tracks are set to 2 days. Fig.1 shows the cyclone numbers for each winter season (DJF) from 1001 to 1990. Average cyclone numbers in each century are shown in Fig. 2. The fewest average cyclone number (201 counts) is in the twentieth century (1900-1990). The next minima of average cyclone numbers (202 counts) are in the thirteenth (1201-1300) and fourteenth (1301-1400) century. Afterward cyclone numbers increase slowly and reach the highest values (206 counts) in the sixteenth (1501-1600) century.

Cyclone tracks are clustered into ten groups by the k-means method. Before clustering, each track path is fitted as a second-order polynomial function of the lifetime of this storm (Chu et al. 2010). Fig. 3 shows the ten track groups. Red tracks denote the centroid track for each group. Histograms for different clusters show that more than 60% of cyclones in the Atlantic and Pacific last 2 to 6 days (Fig. 4a, c). Note that most long-lived (more than 10 days) cyclones are primarily over the western Atlantic (see cluster 9) with over 8% of all cyclones (Fig. 4 a). The climatological histogram of cyclone maximum deepening rates is shown in Fig. 4 b and d. Oceanic cyclones deepen rapidly compared to other cyclones. Cyclones over the Pacific are characterized by greater maximum deepening than in the Atlantic (Fig. 4 b and d). Cyclones of cluster 6 present the highest percentage (34%) on rapid deepening (larger than 10 hPa per 12 h) (Fig. 4 d).

3. Conclusion

The numbers of extratropical storms in winter have strong year to year variations but an obvious trend is not present during the quasi-millennial period (1001-1990). The minimum of average cyclone numbers is in the twentieth century (1901-1990). Cyclones are also less in the thirteenth (1201-1300) and fourteenth (1301-1400) century. Cyclone tracks are clustered into ten groups by the k-means method. Oceanic cyclones characterize the feature of rapid deepening and long lifetime. That also indicates the objective clustering method separates cyclone tracks into groups in a reasonable way.

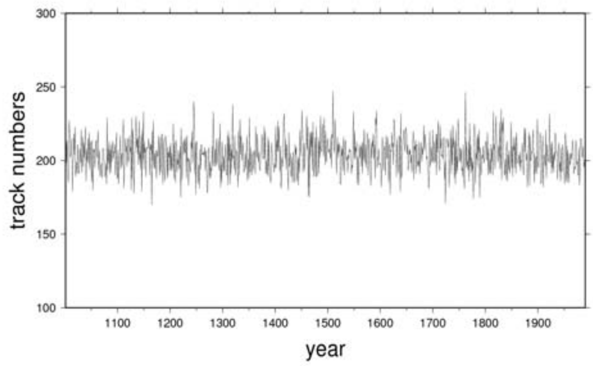

Fig. 1 time series (1001-1990) of annual winter cyclone counts

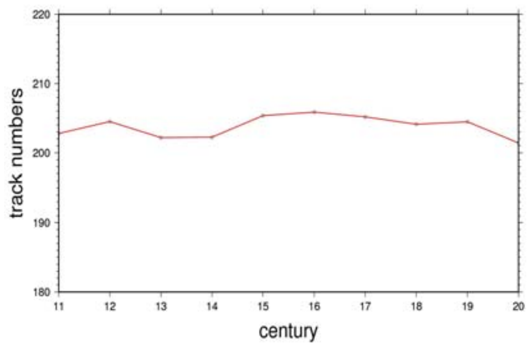

Fig. 2 average cyclone counts in each century

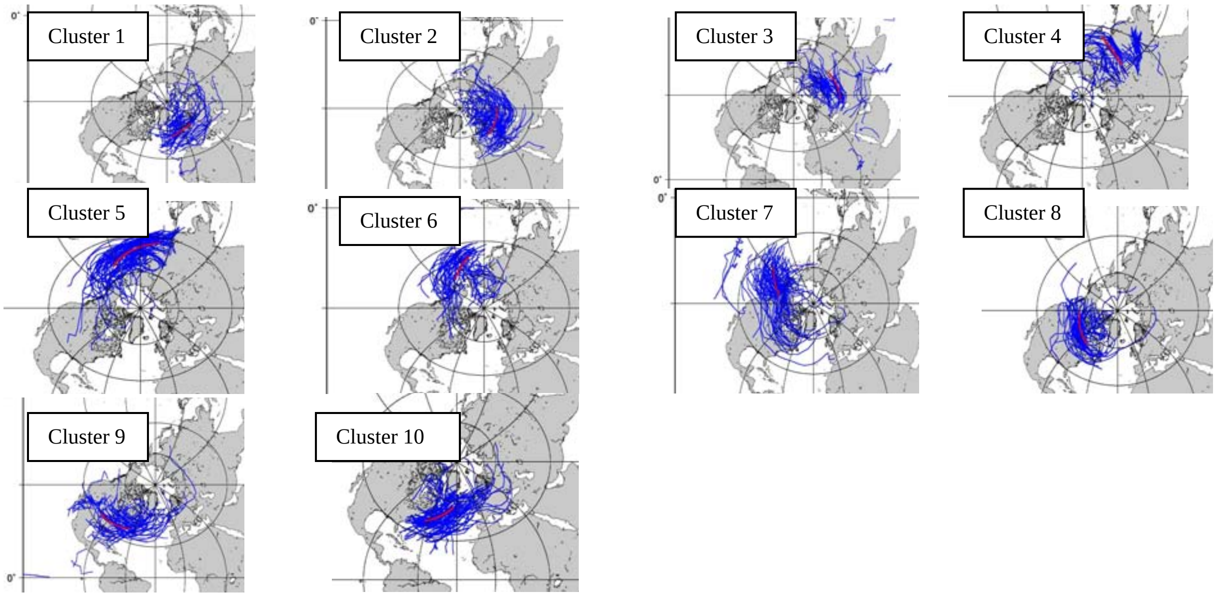

Fig. 3 Northern Hemispherical cyclone tracks clustered by K-mean: members (blue) and centroid (red) of ten clusters

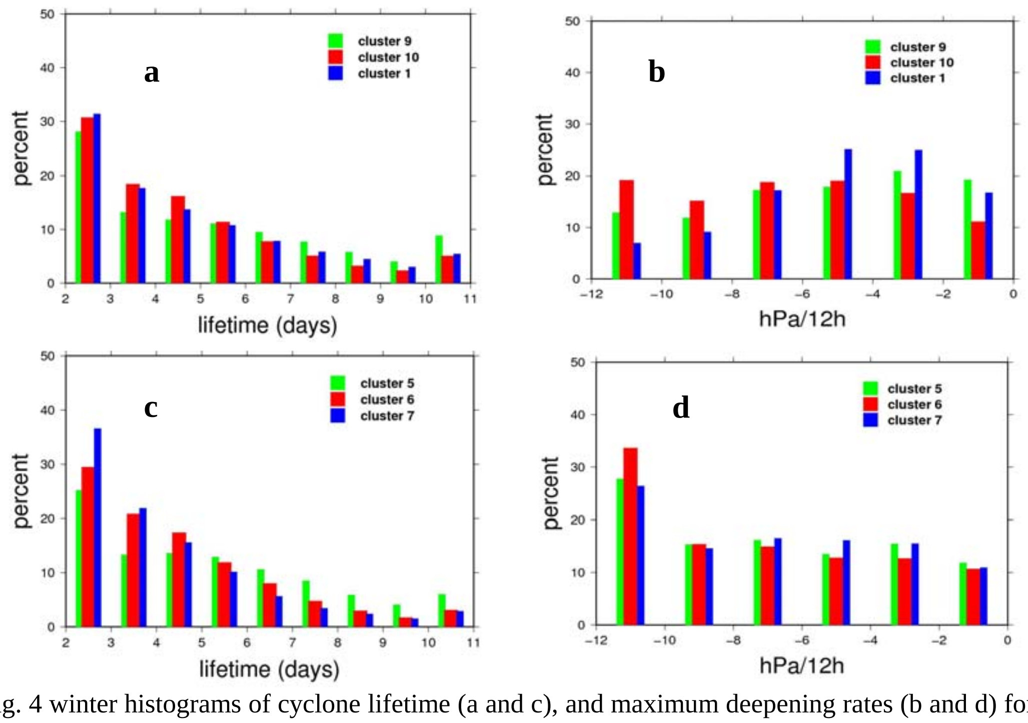

Fig. 4 winter histograms of cyclone lifetime (a and c), and maximum deepening rates (b and d) for cyclones over the Atlantic (a and b) and the Pacific (c and d)

Reference

Chu P., X. Zhao and J. Kim, 2010: Regional typhoon activity as revealed by track patterns and climate change. Hurricanes and Climate Change, 2, 137-148.

Gouirand I., V. Moron and E. Zorita, 2007: Teleconnections between ENSO and North Atlantic in an ECHO-G simulation of the 1000-1990 period. Geophysical research letters, 34, L06705.

Hodges K. I., 1999: Adaptive constraints for feature tracking. Monthly Weather Review, 127, 1362-1373.